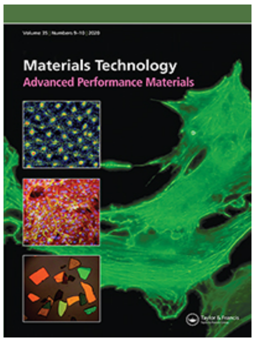

Materials Technology

Advanced Performance Materials

ISSN: (Print) (Online) Journal homepage: https://www.tandfonline.com/loi/ymte20

Ascorbic acid-assisted solvothermal synthesis of LiMn$_{1-x}$Fe$_x$PO$_4$/C nanoparticles for high-performance Li-ion cathode materials

Jing Li , Chaowei Guo , Yuanbin Qin & Xiaohui Ning

To cite this article: Jing Li , Chaowei Guo , Yuanbin Qin & Xiaohui Ning (2020) Ascorbic acid-assisted solvothermal synthesis of LiMn$_{1-x}$Fe$_x$PO$_4$/C nanoparticles for high-performance Li-ion cathode materials, Materials Technology, 35:9-10, 565-571, DOI: 10.1080/10667857.2020.1712533

To link to this article: https://doi.org/10.1080/10667857.2020.1712533

MATERIALS TECHNOLOGY
2020, VOL. 35, NOS. 9–10, 565–571
https://doi.org/10.1080/10667857.2020.1712533

Taylor & Francis
Taylor & Francis Group

Ascorbic acid-assisted solvothermal synthesis of $LiMn_{1-x}Fe_xPO_4/C$ nanoparticles for high-performance Li-ion cathode materials

Jing Li, Chaowei Guo, Yuanbin Qin and Xiaohui Ning

Center for Advancing Materials Performance from the Nanoscale (CAMP-Nano), State Key Laboratory for Mechanical Behavior of Materials, Xi'an Jiaotong University, Xi'an, PR China

ABSTRACT

$LiFePO_4$ is a promising cathode material for lithium-ion batteries due to its excellent rate capability and superior safety. However, its relatively low energy density makes the research efforts towards another olivine structure material $LiMnPO_4$, which exhibits higher energy density and operating voltage. Nevertheless, $LiMnPO_4$ does not show the remarkable electrochemical performance attributing from the low electronic/ionic conductivity. To solve the problems, a facile solvothermal method is used to successfully synthetise the $LiMn_{1-x}Fe_xPO_4/C$ with different Fe/Mn ratio (LMFP/C) nanoparticle in this paper. The length of the obtained $LiMn_{1-x}Fe_xPO_4/C$ is less than 200 nm. Owing to the doping of iron and the nano-structure, the $LiMn_{0.5}Fe_{0.5}PO_4/C$ nanoparticle exhibits high discharge capacities of 153.6, 143.2 and 134.5 mAh g^{-1} at rates 0.1 C, 1 C and 5 C, respectively. Furthermore, the effects of pH on the morphology evolution and electrochemical performance have been also investigated in detail.

ARTICLE HISTORY
Received 11 October 2019
Accepted 28 December 2019

KEYWORDS
Lithium ion battery; solvothermal reaction; cathode; lithium manganese iron phosphate

Introduction

In the past few decades, many works have been done on the design and preparation of high-performance electrode materials for the lithium-ion battery [1–9]. In terms of cathode materials, olivine-structured lithium transition metal phosphates $LiMPO_4$ (M = Mn, Fe, Co, or Ni) have been widely investigated as a typical class of potential cathode materials for lithium-ion batteries, due to the low cost, excellent structural stability, nontoxicity and high environmental compatibility [10–15]. Among them, olivine-structured $LiFePO_4$ can deliver an outstanding lifespan over 3000 cycles [16]. However, it exhibits lower energy density because of its low redox potential of 3.4 V [17–19]. Meanwhile, $LiMnPO_4$ has a higher working potential plateau (4.1 V vs. Li^+/Li) thereby providing 20% higher theoretical energy density than that of $LiFePO_4$. Nevertheless, $LiMnPO_4$ exhibits the lower discharge capacity and the worse rate capability, which could be attributed to its poor electronic conductivity ($<10^{-10}$ S cm^{-1}) and low lithium-ion conductivity ($<10^{-16}$ cm^{-2} s^{-1}) [20,21]. Additionally, the poor cycling stability arises from the Jahn–Teller effect also restricts its application [22]. To overcome these drawbacks, Mn^{2+} in $LiMnPO_4$ was partially substituted by Fe^{2+} to form the solid solution $LiMn_{1-x}Fe_xPO_4$. Hong et al. have successfully synthesised the nanoporous $LiMn_{1-x}Fe_xPO_4$ with different iron concentration by employing the conventional solid-state reaction. The particles with 20% iron content ($LiFe_{0.2}Mn_{0.8}PO_4$) deliver the highest specific capacity of 138 mAh g^{-1}[23]. Xiao et al. reported a facile polymer-assisted mechanical activation method to obtain a series of $LiMn_{1-x}Fe_xPO_4$ ($0 \le x \le 1$) materials. Among them, $LiMn_{0.75}Fe_{0.25}PO_4/C$ shows the highest energy and power density at low current rates [24]. It is well known that the size of $LiMnPO_4$ plays a significant role in the electrochemical performances. Hence, to reduce the particle size to nanoscale is another effective way to suppress the sluggish kinetic and acquire the desired rate capability [25–27].

Additionally, the surface modification by using carbon coating on LMFP materials can also improve its electronic conductivity, and suppress the dissolution of manganese from LMPF into the electrolyte, thereby leading to enhanced electrochemical properties [28–30].

Herein, we report a solvothermal method to synthesis the LMFP/C nanoparticles with different Fe/Mn ratio. The as-synthesised LMFP nanoparticles exhibit the improved lithium storage properties when used as a cathode of Li-ion battery. In addition, we study the influence of the Fe/Mn ratio on the electrochemical properties of LMFP/C nanoparticles.

Experimental

Preparation of LMFP

The LMFP nanoparticles were prepared via the ascorbic acid assisted solvothermal method [30]. Polyethylene

CONTACT Xiaohui Ning xiaohuining@mail.xjtu.edu.cn Center for Advancing Materials Performance from the Nanoscale (CAMP-Nano), State Key Laboratory for Mechanical Behavior of Materials, Xi'an Jiaotong University, Xi'an 710049, PR China

glycol 400 (PEG 400) was mixed with H_3PO_4 in a molar proportion of 4:1 firstly. Then, LiOH solution was dropwise added to the as-prepared mixture with magnetic stirring. Secondly, $MnSO_4$ and $FeSO_4$ solutions were introduced into the system simultaneously at the dropping speed of 2 ml/min. Thirdly, Ammonia was added in the solution to adjust its pH values to 6.5, 8 and 9.5, respectively. Further, the ascorbic acid was introduced to the above mixture under stirring. The mixture was then transferred into a stainless steel autoclave and maintained at 180°C for 12 h. Afterwards, the container was cooled down to room temperature. The product was washed and centrifuged several times using distilled water and ethanol. Then, the product was dried under vacuum at 80°C for 12 h. During the whole processes, the molar ratio of Li:P:(Mn+ Fe) was kept at 3:1:1.

Carbon coating of as prepared LMFP

The LMFP/C nanoparticles were prepared via ball milling method to mix 20 wt% sucrose with LMFP in ethanol. The rotational speed was set as 350 rpm for 4 h. Then, the obtained product was heated at 350°C for 2 h and then annealed at 650°C for 4 h under Ar.

Structure and morphology characterisation

The crystalline structure of the as-prepared LMFP powder was conducted by X-ray diffraction (XRD) measurements with a Bruker D8 Advance diffractometer. The morphology of LMFP was characterised by the field emission scanning electron microscopy (FESEM, Hitachi SU6600) and transmission electron microscopy (TEM, JOEL 2100F). The composition of the sample was analysed by Energy dispersive spectroscopy (EDS) mapping.

Electrochemical measurements

For the electrochemical test, the LMFP powder was assembled into the coin-cell in an argon-filled glove box. The electrode slurry was made by dispersing the active materials, Super P and polyvinylidene fluoride (PVDF) in N-methyl pyrrolidone (NMP) in the weight ratio of 8:1:1 with stirring. Then, the slurry was spread on Al foil and dried at 100°C for 12 h under vacuum. Li foil was used as the counter electrode, and 1M $LiPF_6$ dissolved in a mixed solvent of ethylene carbonate (EC) and dimethyl carbonate (DMC) (1:1 w/w) as the electrolyte. Galvanostatic charge-discharge measurements were carried out within the potential window of 2.0 to 4.5 V at room temperature. Cyclic voltammetry (CV) and electrochemical impedance spectroscopy (EIS) tests were carried out on the electrochemical workstation (CHI 660E, Shanghai Chenhua). CV tests were conducted at different scanning rates from 0.1 to 0.5 mV s^{-1}. EIS measurements were performed over the frequency from 100 kHz to 0.1 Hz.

Results and discussions

The effect of ph value of the reaction precursors

Figure 1(a–c) shows the SEM images of the prepared samples obtained at different pH values. The SEM images reveal that all three samples exhibit rod-like structures consisting of different particle length ranging from 100 to 400 nm. With increasing pH value from 6.5 to 8, the length of the nanoparticles is decreasing from 400 nm to 200 nm. However, when

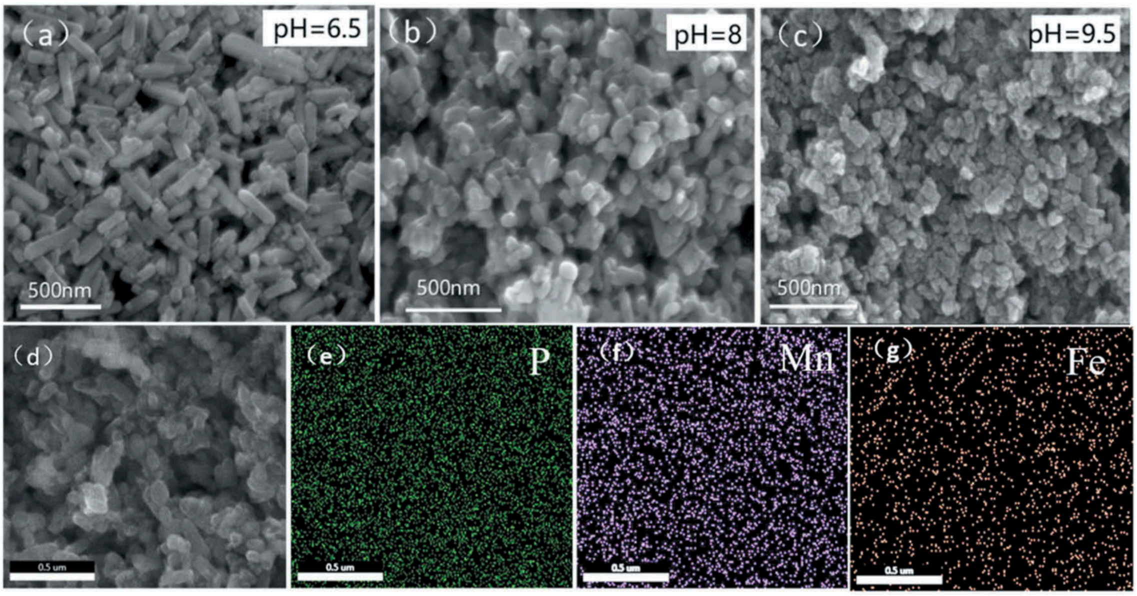

Figure 1. SEM images of $LiMn_{0.8}Fe_{0.2}PO_4$ synthesised at different pH value of the reaction systems: (a) pH = 6.5. (b) pH = 8. (c) pH = 9.5. (d–g) The corresponding EDS mappings of P, Mn, Fe in sample with pH = 8.

the pH value increased to 9.5, it is found that the length of the nanoparticles gets reduced further with severe aggregation phenomena (Figure 1(c)). As seen from Figure 1(d–g), the elemental distribution of P, Mn and Fe of the $LiMn_{0.8}Fe_{0.2}PO_4$ are homogeneous.

To figure out the optimum pH value for the synthesis of LMFP, the electrochemical properties of $LiMn_{0.8}Fe_{0.2}PO_4/C$ nanoparticles prepared at different pH values were also investigated by applying a voltage of about 2–4.5 V at 0.1 C. From Figure 2(a), it is revealed that the reversible discharge capacity of the three samples can reach 121 mAh g^{-1} (pH = 6.5), 132 mAh g^{-1} (pH = 8) and 91 mAh g^{-1} (pH = 9.5), respectively. The samples obtained at pH values of 8 and 6.5 exhibits two voltage plateau at 3.5 V and 4.1 V, which should be related to the redox couples of Fe^{2+}/Fe^{3+} and Mn^{2+}/Mn^{3+}. On the other hand, the profile of the sample obtained at the pH value of 9.5 does not show the voltage plateau at 3.5 V, which may be owing to the fact that the iron gets oxidised easily in an alkaline environment. Figure 2(b) shows the cycling performance of the three samples. The capacity retention rates can reach 96.1% (pH = 6.5), 96.3% (pH = 8) and 90.1% (pH = 9) after 50 cycles at 1 C, respectively. Therefore, from the above results, we can confirm that the optimum pH value is 8 owing to its largest specific capacity and higher capacity retention.

The influence of iron doping

In order to study the influence of the Fe/Mn ratio on LMFP/C nanoparticles, the samples with various Fe/Mn ratios were prepared. The XRD analysis of the as-prepared samples with different Fe/Mn ratio is displayed in Figure 3(a). It can be seen that all the diffraction peaks belong to an olivine-type structure with Pnmb space group and no other noticeable diffraction peaks are found, illustrating the high purity of the samples. Besides, there are no peaks corresponding to carbon, indicating that carbon exists in an amorphous form. It is clearly seen from Figure 3(b), the diffraction peaks slightly shifted towards a higher angle (2 theta) with the increased Fe/Mn ratio. It could be attributed to the reduced unit cell volume because of the smaller radius of Fe^{2+} (0.92 Å) than that of Mn^{2+} (0.97 Å), and these changes in the lattice structure can relieve the interfacial strain between $LiMn_{1-x}Fe_xPO4/Mn_{1-x}Fe_xPO4$ phases, thus it is beneficial to improve the diffusion kinetics of Li^+ in the LMFP/C [31].

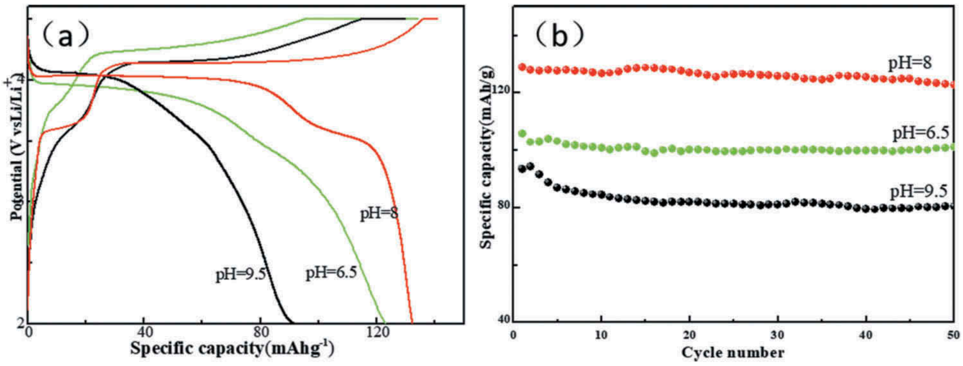

Figure 2. Electrochemical performance of $LiMn_{0.8}Fe_{0.2}PO_4/C$: (a) The first charge/discharge curves of $LiMn_{0.8}Fe_{0.2}PO_4/C$; (b) Cycling performance of $LiMn_{0.8}Fe_{0.2}PO_4/C$.

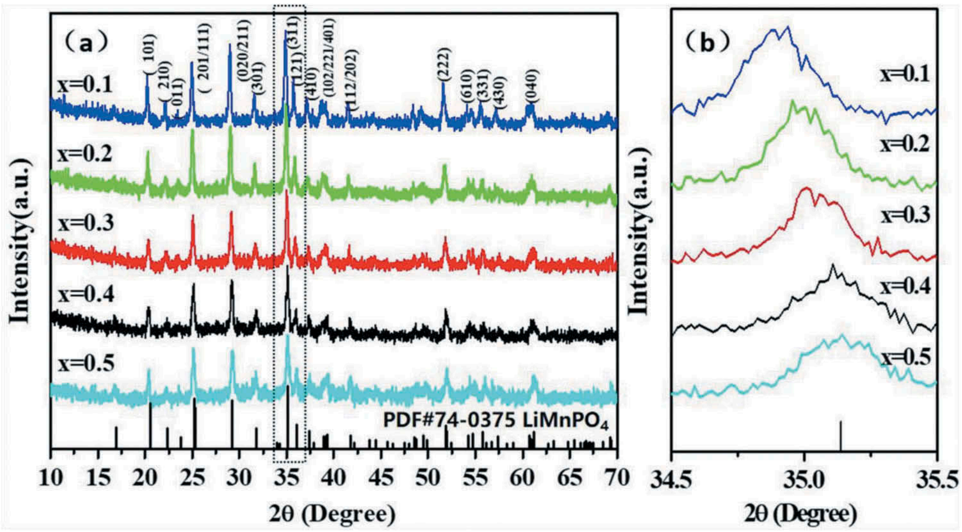

Figure 3. (a) XRD pattern of $LiMn_{1-x}Fe_xPO_4/C$ samples (x = 0, 0.1, 0.2, 0.3, 0.4, 0.5); (b) Detailed XRD patterns of the LMFP/C.

As seen from Figure 4(a–e), the SEM images of LMFP/C with various Fe/Mn ratios show the similar morphology with the length ranging from150 to 200 nm. Moreover, no agglomeration was found in these samples, which is due to the fact that the carbon layer can restricts the further growth of nanoscale LMFP/C during the calcination process. HRTEM was also used to investigate the inner structure, and the results are shown in Figure 4(f). It is notable to see that the particle surface was uniformly coated by a thin carbon layer with a thickness of *ca*. 4 nm. The d-spacing of the lattice fringe are 0.26 and 0.35 nm, corresponding to the (220) and (111) crystal planes of LMFP/C, and the regular lattice fringes reveal the high crystallisation character of the LMFP/C, which is beneficial for enhancing the Li^+ mobility [32]. The uniform nanostructure can provide the short diffusion path for Li^+ and the enlarged contact area between the active materials and the electrolyte. On the other hand, the homogenous carbon coating could ensure the low charge transfer resistance at the LMFP/electrolyte interface, which are both contributing to enhance the redox kinetics of the electrochemical reaction.

Electrochemical performances of LMFP/C were also evaluated. The charge-discharge profiles of LMFP/C nanoparticles with different Fe/Mn ratio are shown in Figure 5(a). It is found that with Fe/Mn ratio increasing, the voltage platform of 3.4 V on the discharge curve becomes longer and flatter along with the increased capacity. Figure 5(b) shows the cycle performances of LMFP/C at 1 C. The capacity retentions after 100 cycles are 95% (Fe/Mn ratio = 5:5), 93% (Fe/Mn ratio = 4:6), 90% Fe/Mn ratio = 3:7), 89% (Fe/Mn ratio = 2:8) and 87% (Fe/Mn ratio = 1:9), respectively. It is obvious that the $LiMn_{0.5}Fe_{0.5}PO_4$/C exhibits the best cycling stability, which is owing to the fact that the substitution of Fe^{2+} to Mn^{2+} in LMFP/C can minimise the dissolution of manganese and inhibit the Jahn–Teller distortion. Figure 5(c) presents the rate capability of LMFP/C at different charge-discharge rate. The reversible specific capacities of $LiMn_{0.5}Fe_{0.5}PO_4$/C nanoparticles are 145.2, 143.2, 137.2 and 134.5 mAh g^{-1} at the rates of 0.5, 1, 2 and 5 C, respectively, showing the best rate capability among the five samples. The superior rate capability is attributed to the minimised polarisation and the improved electronic conductivity arising from the suitable Fe/Mn ratio, the favourable conductive network, and the short ion diffusion path.

Moreover, the performance of energy density at different rates was calculated and is shown in Figure 5(d). The $LiMn_{0.8}Fe_{0.2}PO_4$/C has the highest energy density of 560 Wh kg^{-1} at 0.1 C, which could be attributed to its long plateau at ~4.1 V. During the charging-discharging rate from 0.5 C to 5 C, the energy density of LMFP/C become higher with the increasing of Fe/Mn ratio, owing to the fact that LMFP/C nanoparticles with high Fe/Mn ratio still have good capacity retention at large rates.

To further understand the reason for the improved electrochemical performance of LMFP/C, the CV test of LMFP/C were performed at 0.1 mVs^{-1}, as shown in Figure 6(a). The two pairs of redox peaks of the samples are at 3.3–3.6 V and 4.0–4.2 V, respectively, which is in accordance with the results presented in Figure 2(a). The potential gaps between $Mn^{2+} \rightleftarrows Mn^{3+}$ and $Fe^{2+} \rightleftarrows Fe^{3+}$ redox peaks get decreased as the Fe/Mn ratio increased, owing to the fact that the Fe^{2+} doping can alleviate the polarisation by improving the kinetics of the Li^+ extraction/insertion. The CV tests with different sweep speeds were also carried out for the $LiMn_{0.5}Fe_{0.5}PO_4$ sample, which is shown in Figure 6(c). The peak current (i_p) of the sample and the square root of the scan rate ($v^{1/2}$)

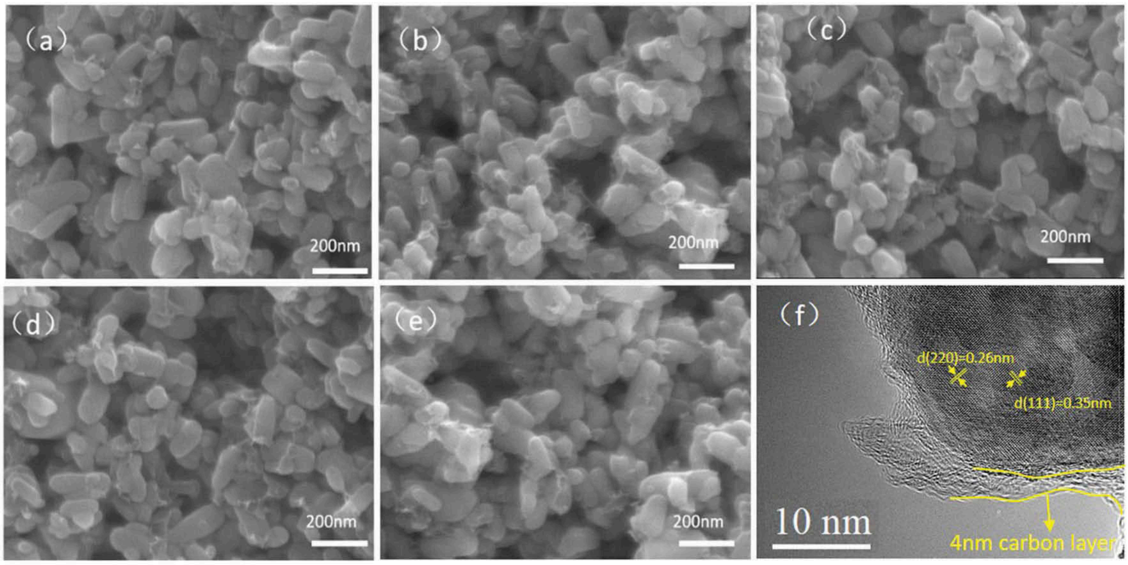

Figure 4. (a–e): SEM images of LMFP/C cathode materials: a) x = 0.1; b) x = 0.2; c) x = 0.3; d) x = 0.4; e) x = 0.5; (f) HRTEM images of $LiMn_{0.5}Fe_{0.5}PO_4$/C.

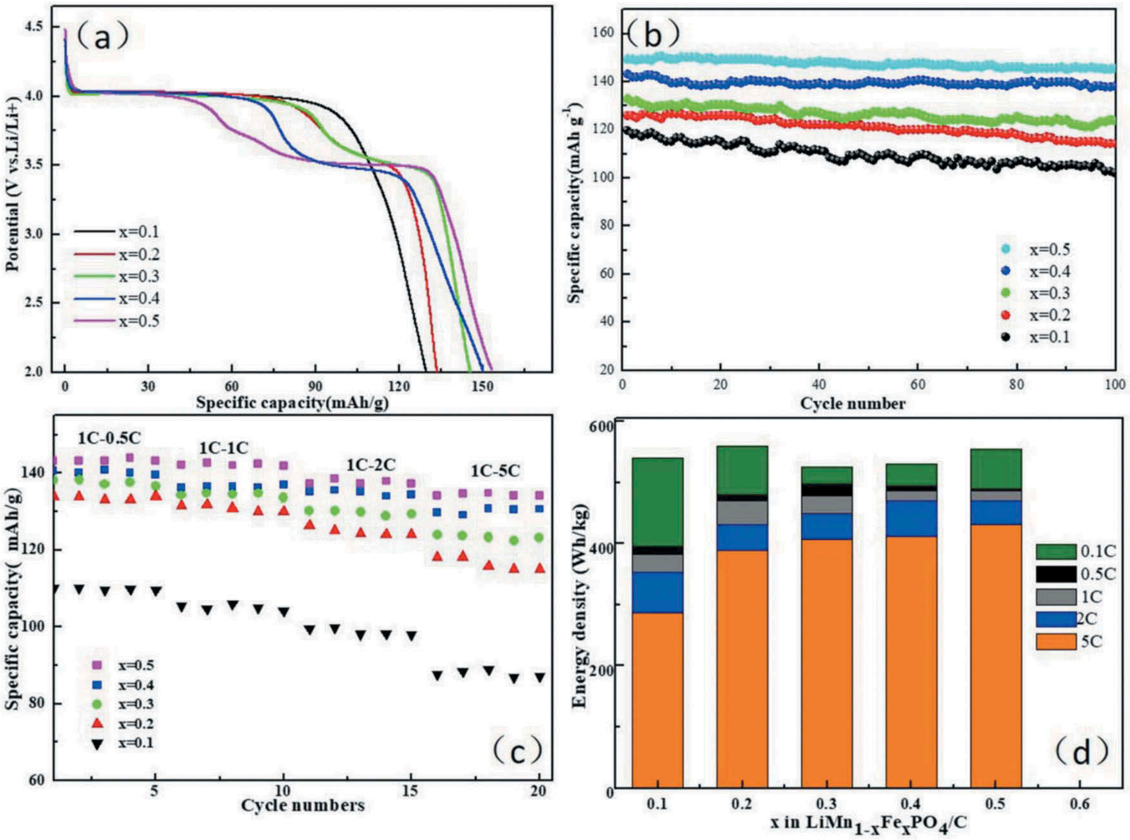

Figure 5. (a) The first charge/discharge curves of LMFP/C; (b) Cycling performance of LMFP/C materials at 1 C; (c) Rate performance and (d) Energy density of LMFP/C at different rates.

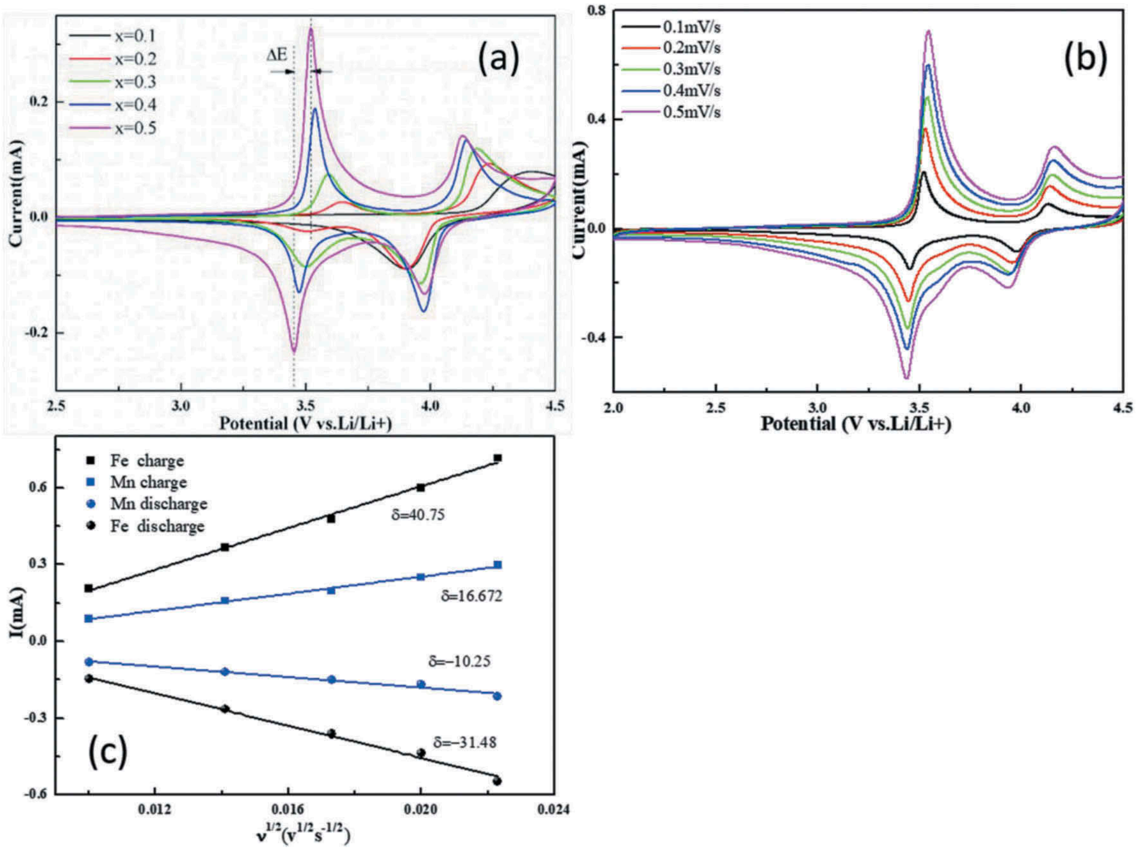

Figure 6. (a) CV curves of LMFP/C at a scanning rate of 0.1 mV s^{-1}; (b) CV test of $LiMn_{0.5}Fe_{0.5}PO_4/C$ at different sweep speeds; (c) Relationship between peak current (i_{p}) and the square root of the scan rate ($\upsilon^{1/2}$).

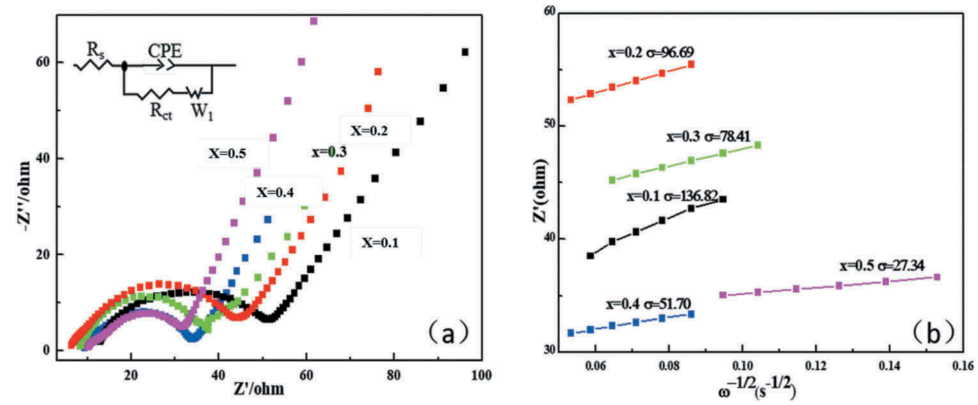

Figure 7. (a) Nyquist plots and (b) the relationship between Z' and $\omega^{-1/2}$ for LMFP/C (x = 0.1, 0.2, 0.3, 0.4, 0.5).

showed a good linear relationship, demonstrating that the electrochemical reaction in LMFP is controlled by the solid-state diffusion of lithium ions.

In order to analysis the interfacial properties between LMFP/C and the electrolyte, the EIS measurement was conducted. Figure 7(a) presents the Nyquist plots of five samples with equivalent circuit inserted. The semicircle in the high-to-middle frequency regime represents the charge transfer resistance (R_{ct}) and the inclined line in the low-frequency regime is associated with the lithium-ion diffusion process. It was found that the R_{ct} became lower as the Fe/Mn ratio increased according to the smaller radius of the semicircle. The D_{Li+} of the five samples can be obtained from the following equation. The Warburg factor σ is equal to the slope between Z' and $\omega^{-1/2}$ in the low-frequency range, and the lithium-ion diffusion coefficient can be calculated according to equation (2).

$$Z' = R_s + R_{ct} + \sigma\omega^{-1/2} \tag{1}$$

$$D_{Li+} = R^2T^2/2A^2n^4F^4C^2\sigma^2 \tag{2}$$

where R is the gas constant, T is the absolute temperature, A is the contact area of the electrode, n is the number of the electrons per molecule, F is the Faraday constant, and C is the concentration of the lithium ion. As shown in Table 1, the D_{Li+} increased as the Fe/Mn ratio increased. From EIS, we can confirm that Fe doping can reduce the charge transfer resistance for the surface reactions and facilitate the Li$^+$ diffusion within the lattice of LMFP/C, which is favourable to achieve the ultrahigh rate capability. These consequences are consistent with the explanation mentioned above.

Table 1. The calculated diffusion coefficient (D_{Li+}) of the LMFP/C (x = 0.1, 0.2, 0.3, 0.4, 0.5).

Sample name	X = 0.1	X = 0.2	X = 0.3	X = 0.4	X = 0.5
R_{ct}(ohm)	44.28	43.27	30.85	28.65	25.37
D_{Li+}(cm^2 s^{-1})	6.3E^{-15}	1.26E^{-14}	1.9E^{-14}	4.4E^{-14}	1.6E^{-13}

Conclusions

In summary, LiMn$_{0.8}$Fe$_{0.2}$PO$_4$/C nanoparticles were successfully synthesised via ascorbic assisted solvothermal method at different pH values. The sample synthesised at pH = 8 shows the highest discharge capacity. More importantly, the LMFP/C materials with different Fe/Mn ratio were prepared. The morphologies of LMFP/C materials show that they exhibit the nano-size of ca. 200 nm with a uniform carbon coating. Among them, the LiMn$_{0.5}$Fe$_{0.5}$PO$_4$/C exhibits a decent capacity of about 154 mAh g^{-1} at 0.1 C. After 100 cycles at 1 C, the capacity retention can reach ~95%. Also, it shows the impressive rate capability of 134.5 mAh g^{-1} at 5 C. Such superior electrochemical performance can be ascribed to the synergistic effect of nanosized particles, the uniform carbon coating, and the suitable Fe/Mn ratio, which are beneficial for enhancing the electron/ion transport kinetics as well as suppressing the Mn^{2+} dissolution. It is believed that our results have an instructive meaning to prepare the LMFP/C nanostructures with a high electrochemical performance which can be used as cathode materials for lithium-ion battery.

Acknowledgments

This work was supported by the grants from National Natural Science Foundation of China (51874228, U1766216). Authors acknowledge the International Joint Laboratory for Micro/Nano Manufacturing and Measurement Technologies for the test service.

Disclosure statement

No potential conflict of interest was reported by the authors.

Funding

This work was supported by the National Natural Science Foundation of China [51874228, U1766216].

References

[1] Fu QF, Li RJ, Zhu XZ, et al. Design, synthesis and lithium-ion storage capability of $Al_{0.5}Nb_{24.5}O_{62}$. J Mater Chem A. 2019;7:19862–19871.

[2] Zhu XZ, Xu J, Luo YP, et al. $MoNb_{12}O_{33}$ as a new anode material for high-capacity, safe, rapid and durable Li^+ storage: structural characteristics, electrochemical properties and working mechanisms. J Mater Chem A. 2019;7:6522–6532.

[3] Zhu XZ, Cao HJ, Li RJ, et al. Zinc niobate materials: crystal structures, energy-storage capabilities and working mechanisms. J Mater Chem A. 2019;7: 25537–25547.

[4] Lou XM, Li RJ, Zhu XZ, et al. New anode material for lithium-ion batteries: Aluminum Niobate ($AlNb_{11}O_{29}$). ACS Appl Mater Interfaces. 2019;11:6089–6096.

[5] Yang LT, Zhu XZ, Li XH, et al. Conductive Copper Niobate: superior Li^+-storage capability and novel Li^+-transport mechanism. Adv Energy Mater. 2019;9:1902174.

[6] Zheng SQ, Liu DM, Tao L, et al. Electrochemistry and redox characterization of rock-salt-type lithium metal oxides $Li_{1+z/3}Ni_{1/2-z/2}Ti_{1/2+z/6}O_2$ for Li-ion batteries. J Alloy Compd. 2019;773:1–10.

[7] Liu YJ, Fan XJ, Zhang ZQ, et al. Enhanced electrochemical performance of Li-rich layered cathode materials by combined Cr doping and $LiAlO_2$ coating. ACS Sustain Chem Eng. 2019;7:225–2235.

[8] Liu DM, Fan XJ, Li ZH, et al. A cation/anion co-doped $Li_{1.12}Na_{0.08}Ni_{0.2}Mn_{0.6}O_{1.95}F_{0.05}$ cathode for lithium ion batteries. Nano Energy. 2019;58: 786–796.

[9] Zheng SQ, Dou AC, Su MR, et al. Influence of Nb doping on electrochemical performance of nanostructured cation disordered $Li_{1+x/100}Ni_{1/2-x/100}Ti_{1/2-x/100}Nb_{x/100}O_2$ composites cathode for Li-ion batteries. J Nanosci Nanotechnol. 2020;20:452–459.

[10] Padhi AK, Nanjundaswamy KS, Goodenough JB, et al. Phospho-olivines as positive-electrode materials for rechargeable lithium batteries. J Electrochem Soc. 1997;144:1188–1194.

[11] Chung SY, Blocking JT, Chiang YM, et al. Electronically conductive phospho-olivines as lithium storage electrodes. Nat Mater. 2002;1:123–128.

[12] Xu YN, Ching WY, Chiang Y-M, et al. Comparative studies of the electronic structure of $LiFePO_4$, $FePO_4$, Li_3PO_4, $LiMnPO_4$, $LiCoPO_4$, and $LiNiPO_4$. J Appl Phys. 2004;95:6583–6585.

[13] Fisher CJ, Hart Prieto VM, Islam MS, et al. Lithium battery materials $LiMPO_4$ (M = Mn, Fe, Co, and Ni): insights into defect association, transport mechanisms, and doping behavior. Chem Mater. 2008;20:5907–5915.

[14] Fergus JW. Recent developments in cathode materials for lithium ion batteries. J Power Sources. 2010;195:939–954.

[15] You X, Xiao S, Zhang T, et al. Effects of chelating agents on electrochemical properties of $Li_3V_2(PO4)_3$/C cathode materials. Mater Technol. 2015;30:64–69.

[16] Wu G, Liu N, Gao XG, et al. A hydrothermally synthesized $LiFePO_4$/C composite with superior low-temperature performance and cycle life. Appl Surf Sci. 2018;435:1329–1336.

[17] Delacourt C, Laffont L, Bouchet R, et al. Toward understanding of electrical limitations (electronic, ionic) in $LiMPO_4$ (M=Fe, Mn) electrode materials. J Electrochem Soc. 2005;152:A913–A921.

[18] Amin R, Balaya P, Maier J, et al. Anisotropy of electronic and ionic transport in $LiFePO_4$ single crystals. Electrochem Solid-State Lett. 2007;10:A13–A16.

[19] Bai N, Xiang K, Zhou W, et al. Hierarchical porous $LiFePO_4$/Carbon composite electrodes for lithium-ion batteries. Mater Technol. 2016;32:203–209.

[20] Deng Y, Yang C, Zou K, et al. Recent advances of Mn-rich $LiFe_{1-y}Mn_yPO_4$(0.5 ≤ y< 1.0) cathode materials for high energy density lithium ion batteries. Adv Energy Mater. 2017;7:1601958.

[21] Norberg NS, Kostecki R. The degradation mechanism of a composite $LiMnPO_4$ cathode. J Electro Soc. 2012;159:A1431–A1434.

[22] Aravindan V, Gnanaraj J, Lee YS, et al. $LiMnPO_4$: a next-generation cathode material for lithium-ion batteries. J Mater Chem A. 2013;1:3518–3539.

[23] Hong J, Wang F, Wang XL, et al. $LiFe_xMn_{1-x}PO_4$: a cathode for lithium-ion batteries. J Power Sources. 2011;196:3659–3663.

[24] Xiao PF, Ding B, Lai MO, et al. High performance $LiMn_{1-x}Fe_xPO_4$(0≤ x≤1) synthesized via a facile polymer-assisted mechanical activation. J Electro Soc. 2013;160:A918–A926.

[25] Fan JM, Yu Y, Wang Y, et al. Nonaqueous synthesis of nano-sized $LiMnPO_4$@C as a cathode material for high performance lithium ion batteries. Electrochim Acta. 2016;194:52–58.

[26] Zhou X, Xie Y, Deng F, et al. The enhanced rate performance of $LiFe_{0.5}Mn_{0.5}PO_4$/C cathode material via synergistic strategies of surfactant-assisted solid state method and carbon coating. J Mater Chem A. 2015;3:996–1004.

[27] Wi SG, Kim JW, Lee SH, et al. Synthesis of $LiMn_{0.8}Fe_{0.2}PO_4$ mesocrystals for high-performance Li-ion cathode materials. Electrochim Acta. 2016;21: 203–210.

[28] Wang C, Li SH, Han YY, et al. Assembly of LiMnPO4 nanoplates into microclusters as a high-performance cathode in lithium-ion batteries. ACS Appl Mater Inter. 2017;9:27618–27624.

[29] Zou BK, Wang HY, Qiang ZY, et al. Mixed-carbon-coated $LiMn_{0.4}Fe_{0.6}PO_4$ nanopowders with excellent high rate and low temperature performances for lithium-ion batteries. Electrochim Acta. 2016; 196:377–385.

[30] Zuo PJ, Cheng GY, Wang LG, et al. Ascorbic acid-assisted solvothermal synthesis of $LiMn_{0.9}Fe_{0.1}PO_4$/C nanoplatelets with enhanced electrochemical performance for lithium ion batteries. J Power Sources. 2013;243:872–879.

[31] Wang Y, Yang H, Wu CY, et al. Facile and controllable one-pot synthesis of nickel-doped $LiMn_{0.8}Fe_{0.2}PO_4$ nanosheets as high performance cathode materials for lithium-ion batteries. J Mater Chem A. 2017;5:18674–18683.

[32] Zu PJ, Wan LG, Zhang W, et al. A novel nanoporous Fe-doped lithium manganese phosphate material with superior long-term cycling stability for lithium-ion batteries. Nanoscale. 2015;7:11509–11514.